ORIGINAL ARTICLE

lajss.org© Latin American Journal of Solids and Structures

www.lajss.org

A revised theoretical model for external inversion process over a circular die

Wanqi Zhang[a], Guansheng Yin[a,b]*, Minghui Shi[a], Pengfei Wei[a], Jianqiang Wang[c], Junkai Zhao[d]

[a] School of Science, Chang'an University, Xi'an 710064, China. Email: 2018012001@chd.edu.cn, yings@chd.edu.cn, 2017012001@chd.edu.cn, 2015012002@chd.edu.cn

[b] School of traffic Engineering, Xi'an Vocational University Of Automobile, Xi'an 710600, China. Email: yings@chd.edu.cn

[c] CCCC Civil Engineering Science & Technology Co. Ltd. Xi'an 710075, China. Email: 416746848@qq.com

[d] School of Metallurgical Engineering, Xi'an University of Architecture and Technology, Xi'an 710055, China. Email: jk86@xauat.edu.cn

* Corresponding author

https://doi.org/10.1590/1679-78257973

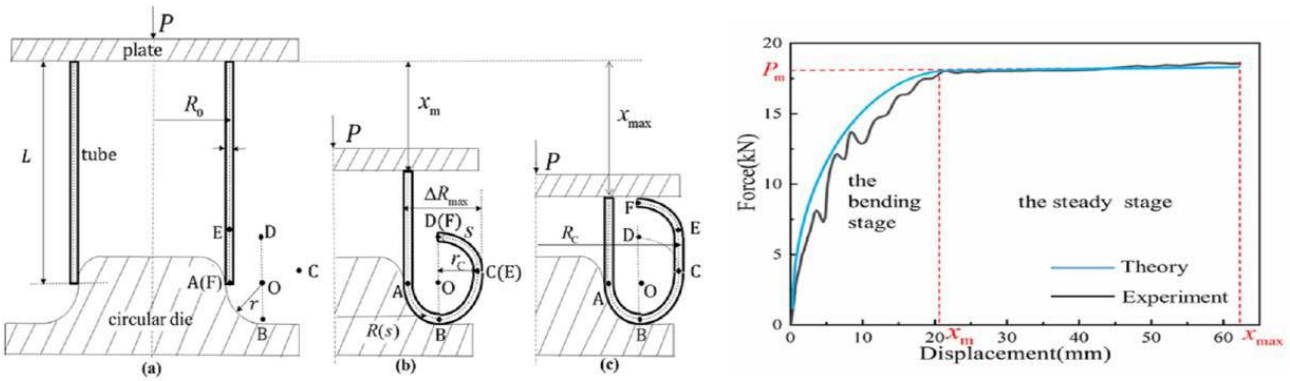
Abstract

As an ideal impact energy absorber, the external inversion process of thin-walled metal tubes over circular dies has been studied theoretically since 1960s. However, in the most existing theoretical models, the curvature in the deformation area is a constant and only the steady inversion force is studied. Limited research has been conducted on the whole inversion process. In this study, from experimental and numerical results, the curvature is found to be varying and the whole inversion process can be divided into two stages by three states. Then a modified geometric model is proposed and the force displacement curves is derived. Next, it has been observed that current theoretical results exhibit greater conformity with experimental and numerical results. Finally, the effects of the tube wall thickness, tube average radius and die radius on crashworthiness indicators are studied theoretically by the verified theoretical model. These outcomes offer valuable reference for further research on tube inversion forming and energy absorption characteristics of external inversion mode.

Keywords

Inversion tube, Energy absorption, Theoretical model, The steady inversion force

Graphical Abstract



Received: December 21, 2023. In revised form: January 17, 2024. Accepted: January 23, 2024. Available online: January 25, 2024.
https://doi.org/10.1590/1679-78257973

Latin American Journal of Solids and Structures. ISSN 1679-7825. Copyright © 2024. This is an Open Access article distributed under the terms of the Creative Commons Attribution License, which permits unrestricted use, distribution, and reproduction in any medium, provided the original work is properly cited.

1 INTRODUCTION

By virtue of the lightweight nature and high efficiency of thin-walled metallic structures, the utilization of thin-walled tubes as energy-absorbing devices has been widely adopted in vehicle, railway, aerospace and ship-building industries (Fauzan Djamaluddin (2023)). Many studies have been performed to identify the characteristics of thin-walled tubes (Ruyang et al. (2023)). In particular, circular tubes have been widely used due to their good energy absorption rate per unit mass (Amirhosein et al. (2022)). The plastic failure modes of a thin-walled metal circular tube under axial compression can be divided into progressive buckling, global buckling, inversion, expansion, splitting and shrinking according to the geometry and the boundary conditions of the tube.

One of the main weaknesses of traditional progressive buckling mode is the transfer of sudden initial peak load and loads that fluctuate frequently to the main structure and passengers. Hence, different methods carried out to decrease initial peak loads and create uniformity of compressing force, such as grooved, corrugated and holes. However, inversion mode has the steady inversion force and does not have excessive initial peak load (QIU Xinming et al. (2016)). Therefore, inversion tubes are widely used in the design of energy absorbers, e.g.in aerospace and automobile engineering (Magrinho et al. (2019)). The inversion mode can be categorized into two modes: free inversion and inversion over a die, based on whether the deformation area is subjected to stress or not. And the inversion over a die can be categorized into two types based on the shape of the die: the inversion over a circular die and the inversion over a conical die. Additionally, it can also be classified as external or internal inversion depending on the direction of the inversion. In the present paper, only the external inversion over a circular die is studied.

The reliability of theoretical analysis relies on the geometric model that can accurately depict the deformation characteristics of the inversion process. And for the sake of simplicity, the geometric model with constant curvature in deformation area are adopted in most previous analytical model. Al-Hassani et al. (1972) proposed the earliest analytical model that only predicted the steady external inversion load. Huang and Yu (1996) and Luo et al. (2003) carried out the expressions of the external steady inversion force by the equilibrium equations. Niknejad and Moeinifard (2012) obtained the external steady inversion force expression by energy method. Several attempts have been made to modify the geometric model to improve the accuracy of theoretical analysis. Leu (2000) proposed a geometric model in which the meridional curvature changes instantaneously at separation from the die. However, the author still opted to use the conventional geometric model with constant curvature due to the complexity involved in obtaining the curvature of this geometric model. Yu et al. (2016) utilized the geometric model proposed by Leu (2000) and derived the theoretical expressions of the steady inversion force and the forming radius by energy method.

Most previous theoretical studies of inversion mode are only aimed at obtaining the steady inversion force. Little research has been done to obtain the force-displacement curves of the whole inversion force which can reflect the inversion force before the steady state and the maximum inversion displacement. Miscow and Al-Qureshi (1997) proposed the inversion load expression of the whole inversion process. However, an initial peak load that predicted by the expression was larger than the steady inversion force, which is inconsistent with the experimental results. Niknejad and Moeinifard (2012) divided the inversion process into three stages. However, neither of the two above theoretical studies can obtain the maximum displacement indicating the end of the steady state.

The geometric model employed in the existing theoretical analysis is oversimplified and fails to accurately capture the deformation characteristics of the inversion process obtained from the experiments. And limited research has been conducted on the whole inversion process. To investigate the deformation profile and the deformation stages, the experiment and numerical simulation are conducted first. Then, a revised theoretical model considering curvature change in deformation area will be established based on the experiment and numerical results. Finally, the prediction of current model will be validated and discussed.

2 EXPERIMENT AND NUMERICAL SIMULATION

2.1 Problem Description

An original circular tube, as shown in Figure 1a, with initial height L, initial wall thickness t_0 and initial average radius R_0 is compressed along the axial direction under force *P*, over a circular die with radius r. The displacement of the top plate is represented by *x* as the tube undergoes inversion. After inversion, the distance between the outer tube's outside radius and the inner tube's inside radius is denoted as the maximum radius difference ΔR_{max}. And the curvature radius of point C is defined as the forming radius r_C

$$r_C = \Delta R_{max} - r - 0.5t_0 \tag{1}$$

Previous theoretical studies (Al-Hassani et al. (1972), Huang and Yu (1996), Luo et al. (2003), Niknejad and Moeinifard (2012)) commonly assumed a constant curvature in the deformation region $\overset{\frown}{AD}$, resulting in a forming radius

$$(r_C)_C = r - 0.5t_0 \tag{2}$$

Yu et al. (2016) assumed that both $\overset{\frown}{AB}$ and $\overset{\frown}{BC}$ segments are quarter circles with different radii, that is, the curvature radius at point B changed immediately. And the curvature radius of $\overset{\frown}{BC}$ segment is determined as follows,

$$(r_C)_Y = \frac{t_0}{2} \cdot \sqrt{\frac{R_0 + r - 0.5t_0}{t_0}} \tag{3}$$

2.2 Experiment

In this study, three types of circular 6063 aluminum tubes, A, B, and C, with various average radii and thicknesses (Figure 2) are investigated. The purchased tubes were cut into the length of 100mm. Quasi-static axial inversion tests were carried out using a CMT5305 test machine to investigate the external inversion behaviors of circular tubes over circular dies. The tube was sandwiched between the top plate and the bottom circular die for the axial compression tests, as illustrated in Figure 1b. A constant speed of 2 mm/min was utilized to ensure the tests be in a quasistatic state (Wang et al. (2021)). Lubricating oil and graphite powder were used as lubricants throughout the experiments. Table 1 presents a summary of the experimental work plan. For the convenience of discussion, the test is named based on the type of tube, the radius of the die and the inversion direction. For instance, Ar3EX manifests that external inversion process of the tube A over a die with radius 3mm. Then four tests were conducted with each test was repeated three times to ensure statistical meaning. During the crushing process, the compression force and the displacement data were simultaneously recorded from the test machine. Having completed the experiments, the specimens were sectioned along their central axis to facilitate measurement of the maximum radius difference.

Three tensile coupons (Figure 3) from each type of circular tubes were sectioned from the purchase tubes walls by wire cutting as ASTME8 standard (Song et al. (2021)). The uniaxial tensile tests were carried out on a UTM6503 test machine at the speed of 2 mm/min. In order to control the results of the tensile tests, three samples were taken for each test. The engineering stress-strain curves of each specimen were shown in Figure 4. The different mechanical properties of each type of tubes are summarized in Table 2.

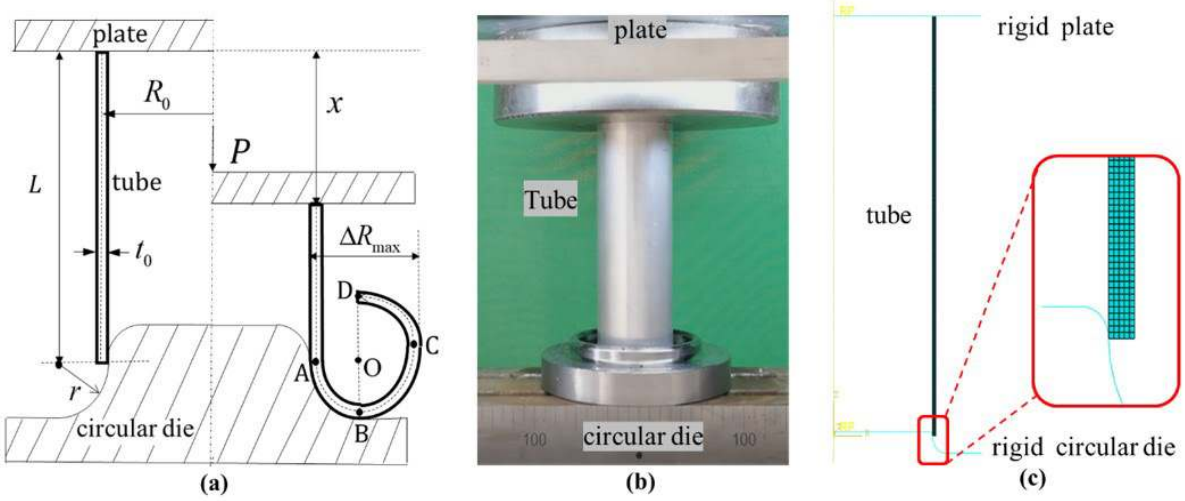


Figure 1 Schematic for an external inversion process over a circular die:(a) axial profile; (b) schematic of test setup; (c) Numerical mode.



Figure 2 Specimens for experiments.

Table 1 Summary of the experimental work plan.

Test case	Tubes			r
	R_0 (mm)	t_0 (mm)	L(mm)	(mm)
Ar3EX	19.5	1	100	3
Ar4EX	19.5	1	100	4
Br3EX	22	1	100	3
Cr3EX	33.4	1.2	100	3

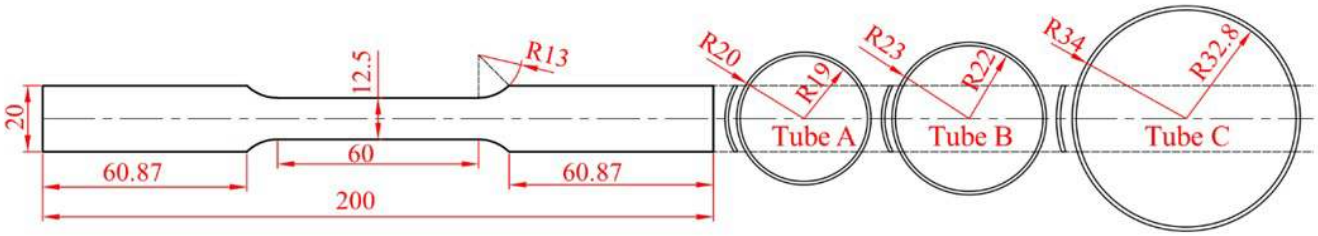


Figure 3 The dimentions of tensile speciments (mm).

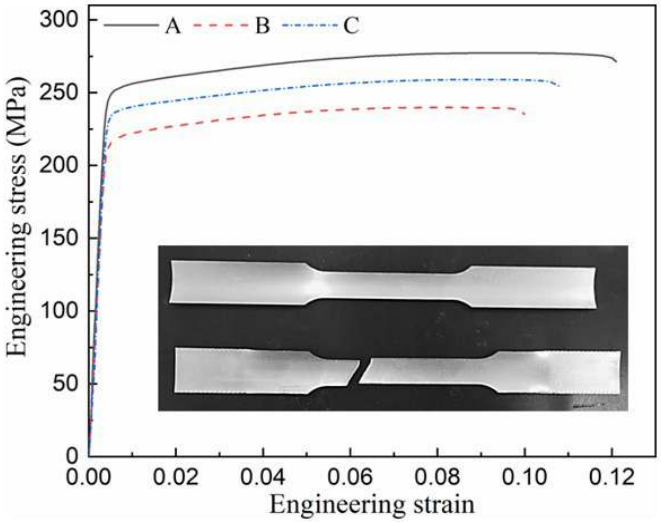


Figure 4 The engineering stress-strain curves of three 6063 aliminiun tubes.

Table 2 Material properties of the aluminum tubes.

Material	density ρ / (kg·m^{-3})	Young's modulus E / GPa	Yield stress σ_s / MPa	Ultimate stress σ_u / MPa	Poisson's ratio μ
A	2758	64	224	277	0.3
B	2690	55	210	240	0.3
C	2700	57.5	220	260	0.3

2.3 Numerical Simulation

The tube inversion processes were simulated using the finite element software Abaqus. On account of rotational symmetry of the deformation modes shown in experimental results, the axisymmetric geometry of the model was created, as shown in Figure 1c. The aluminum circular tubes were modeled with 4-node bilinear axisymmetric quadrilateral elements with reduced integration (CAX4R) and 2-node linear axisymmetric rigid link elements (RAX2) was used for the top rigid plate and the bottom rigid die. The true stress-strain curves for the aluminum materials obtained from the above experiments were used in numerical simulations and the strain rate effect can be neglected due to the aluminum alloys generally show low strain-rate sensitivity for low-speed compression (Tan et al. (2023)). All translational and rotational degrees freedom of the bottom die were constrained, while the top rigid plate was only unconstrained along the axial direction and displaced towards the rigid circular die. The loading speed was superficially ramped up to 1 m/s to accelerate the computation. This speed was adequate as the kinematic energies were well below 5% of the total energy so that the simulations could be regarded as quasi-static (Qiu et al. (2023). To obtain the appropriate value of friction coefficient f between the die and the tube interface, various values for f were tested. It was found that the force displacement curve obtained from the FE model with a friction coefficient 0.15 matched the best with the experimental curve in terms of both the shape of curve and magnitudes of the peaks. Therefore, the value of the friction coefficient f=0.15 was assumed for the subsequent study.

2.4 Experimental and Numerical Results

The force-displacement curve of sample Ar3EX and the corresponding deformation modes at four typical moments are illustrated in Figure 5. As depicted in Figure 5a, the force displacement curve obtained by simulation exhibits excellent agreement with the experimental results. At the beginning of the inversion process, there are several local peak loads in Figure 5a and the deformation modes corresponding to the first local peak force (Imoment) and the first local trough force (II moment) are shown in Figure 5b. This phenomenon can be attributed to the existence of a gap between the tube and die. However, the influence of these local peak forces on the energy absorption characteristics of the inversion mode can be ignored because these peak forces are all smaller than the subsequent platform force. The inversion process can be divided into two stages, namely, the bending stage and the steady stage according to the force displacement curve obtained by experiment and simulation. And the displacement values of 0, x_m and x_{max} correspond to the initial, critical (III moment), and final states (IV moment) of the inversion process, respectively. During the steady stage, the inversion force remains constant, namely, the steady inversion force P_m.

To simplify calculations and accurately fit experimental results, it is assumed that the relationship between inversion force and displacement follows a quadratic function before reaching critical state. Subsequently, the relationship between the inversion force and displacement in the whole external inversion process can be described that,

$$P(x)=\begin{cases}-\dfrac{P_m}{x_m^{\,2}}(x-x_m)^2+P_m & x\le x_m\\ P_m & x_m<x\le x_{max}\end{cases} \tag{4}$$

And the theoretical analysis will provide the expressions for the critical displacement x_m, the maximum displacement x_{max} and the steady inversion force P_m.

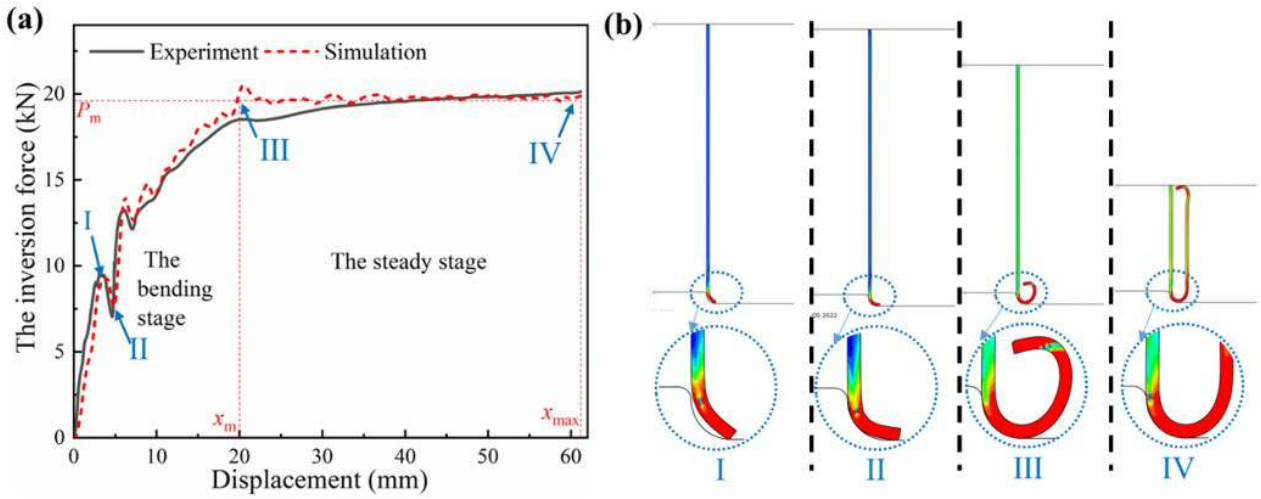


Figure 5 The force displacement curves and the deformation mode for sample Ar3EX:(a) The force displacement curves; (b)The deformation mode

The forming radius obtained by previous theoretical analysis and current experiments are shown in Table 3. It can be found that both the forming radii $(r_C)_C$ and $(r_C)_L$ have large errors with the experimental results. And it can be seen from Table 3 that the forming radius obtained by numerical simulation is closer to the experimental results than obtained by Eq. (2) and Eq. (3). Comparisons of the experimental and simulation results for the maximun displacement and the steady inversion force are listed in Table 4. Similarly, the numerical results can well predict the experimental results. Therefore, the numerical model established in this paper can be used to describe the deformation mode and inversion force of the inversion process.

Table 3 Comparisons of current experimental results, previous theoretical and current numerical results for the forming radius

Test case	The forming radius (mm)			
	Exp.	$(r_C)_C$ (error%)	$(r_C)_L$ (error%)	Simu. (error%)
Ar3EX	2.9	2.5(13.79)	2.35(18.97)	3.24(11.72)
Ar4EX	3.4	3.5(2.94)	2.4(29.41)	3.60(5.88)
Br3EX	3.1	2.5(19.35)	2.5(19.35)	3.33(7.42)
Cr3EX	3.6	2.5(30.56)	3.28(8.89)	3.55(1.39)

Table 4 Comparisons of the experimental and simulation results for the maximun displacement and the steady inversion force

Test case	The maximum displacement (mm)		The steady inversion force (kN)	
	Exp.	Theo. (error%)	Simu.	Theo. (error%)
Ar3EX	61.1	61.35(0.41)	17.8	20.30(14.04)
Ar4EX	62.3	62.9(0.96)	18.4	18.98(3.15)
Br3EX	59.2	61.05(3.13)	18.9	18.78(0.63)
Cr3EX	60.8	60.63(0.28)	35.2	36.25(2.98)

3 THEORETICAL MODEL

3.1 The Determination of The Geometric Model

Based on the above experimental and numerical results, a novel geometric model is proposed to describe the overturning deformation mode. As shown in Figure 1, the external inversion process was divided into two stages by three states: the bending stage between the initial state and the critical state, and the steady stage between the critical state and the final state. The points A, B, C denote the starting point of deformation, the point of separation from the die, and the point of deformation termination, respectively. For simplicity, the following basic assumptions are adopted for the geometric model of external inversion process:

(1) The tube has intimate contact with the die throughout the segment $\overset{\frown}{AB}$.

(2) Tube thickness and height are both remain constant during the external inversion process.

(3) Only the steady inversion condition of the tube is taken into consideration, while two failure modes, namely progressive buckling and cracking caused by unreasonable tube size, initial material defect and die radius are excluded from consideration.

At the initial state (Figure 6a), the two points A and F are spatially coincident. Then the tube tip F begins to curl until the critical state of the inversion process is reached (Figure 6b). At this state, the two points C and E coincide in space as well as the points D and F, and the displacement of the upper end of the tube is defined as the critical displacement x_m . After that, the inversion process enters the steady stage. There is no deformation in section $\overset{\frown}{EF}$, the tube is unbending at point C, and the section CE is parallel to the initial tube wall in the steady stage. The final state will be reached until the tube tip F contacts the upper plate (Figure 6c), the inversion force increases sharply instantly. And the displacement of the upper end of the tube at this moment is defined as the maximum displacement x_{max} . The coordinate system *s* shows the position of the tube relative to the initial position (point A), and it is defined along the tube axis.

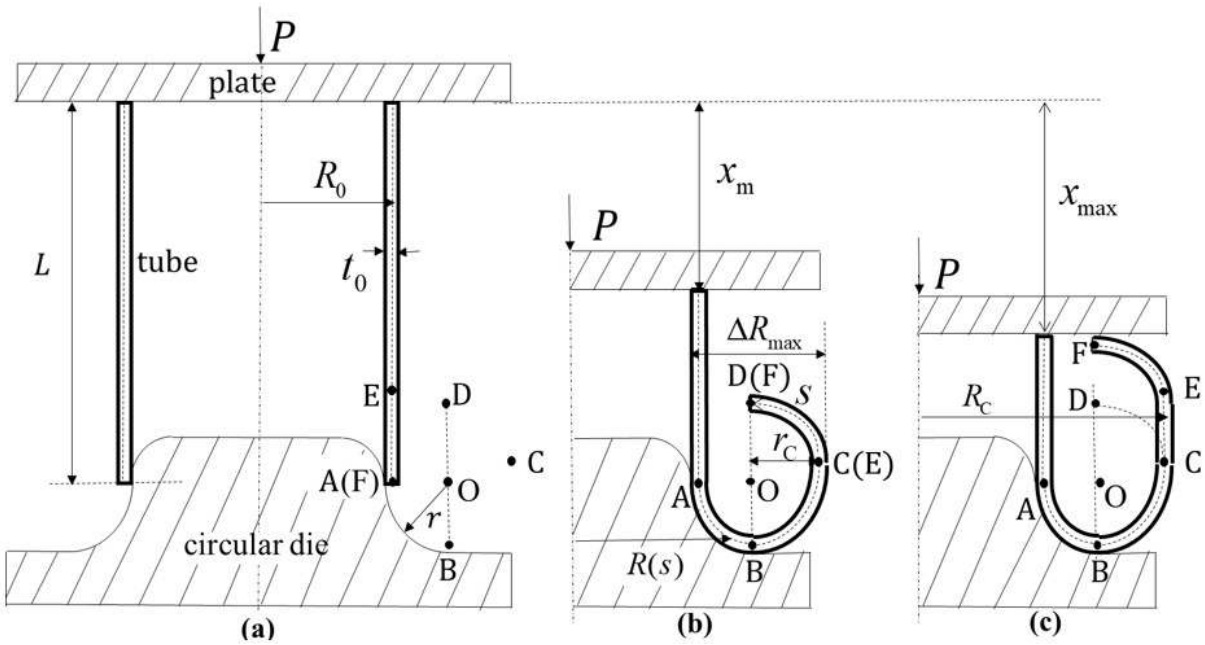


Figure 6 Axial profile of geometrical model for an external inversion process over a circular die: (a)the initial state (b)the critical state (c)the final state.

The initial bending radius of point A is only related to the die radius *r* and the tube initial thickness t_0 .

$$r_A = r - 0.5t_0 \tag{5}$$

So that the curvature of point A is $\kappa_A = 1/r_A$.

Because the tube wall thickness is assumed to remain constant during the external inversion process, the AB segment is a quarter arc segment of constant curvature κ_A . According to the curvature variation of the deformation region obtained by numerical simulation,, it is assumed that the curvature is linearly distributed in both $\overset{\frown}{BC}$ and $\overset{\frown}{CD}$ ($\overset{\frown}{EF}$) segments, that is the segment $\overset{\frown}{BC}$ is a curve where the curvature gradually changes from κ_A (at point B) to κ_C (at point C), the segment $\overset{\frown}{CD}$ ($\overset{\frown}{EF}$) decreases from κ_C (at point C) to zero(at point D).

3.1.1 The Forming Radius

The forming radius is an important geometric parameter to describe the deformation characteristics of the inversion mode, which is also the basis for accurately predicting the critical displacement, the maximum displacement and the steady inversion force. The critical states of the three previous different geometric models for the external inversion process are shown in Figure 7, where the four points A, B, C and D are defined identically to those in Figure 6.

Figure 7a is the simplest and most widely used geometric model for external inversion process (Huang and Yu (1996)), which assumes that the segment $\overset{\frown}{AD}$ is a three-quarters circle with constant curvature. The geometric model (Niknejad and Moeinifard (2012)) shown in Figure 7b assumes that the segment $\overset{\frown}{AD}$ is a circle with constant curvature without considering the curvature change of the $\overset{\frown}{AD}$ segment caused by the spatial non-coincidence of A and D points. The forming radius of these two geometric models is $(r_C)_C$ obtained by Eq. (2). Yu et al. (2016) adopted the geometric model shown in Figure 7c. The forming radius of this geometric model is $(r_C)_Y$ obtained by Eq. (3).

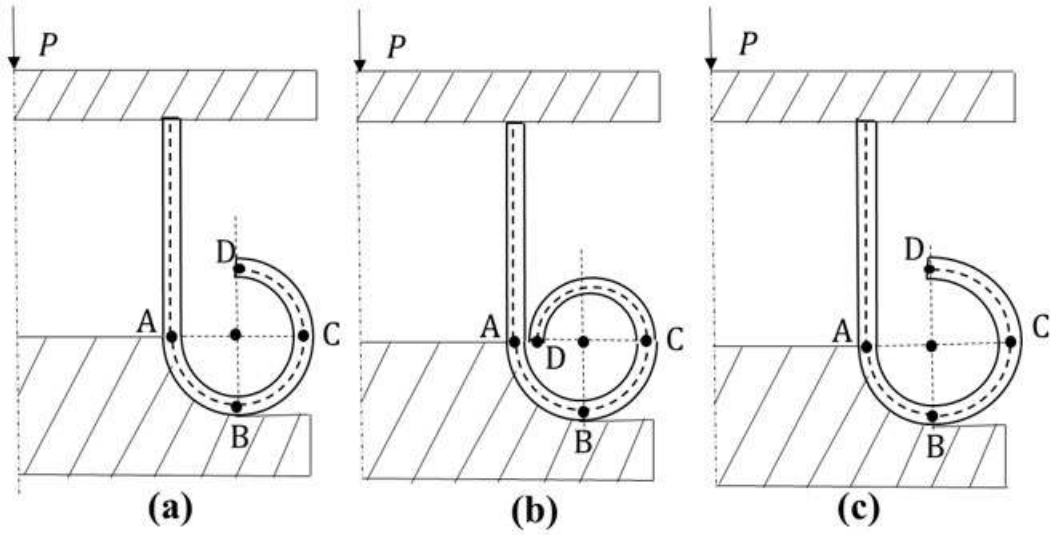


Figure 7 The critical state of different geometric models for inversion process over a circular die: (a) Huang and Yu (1996) (b) Niknejad and Moeinifard (2012) (c) Yu et al. (2016).

It has been explained in Section 3.1 that the forming radius obtained by Eq. (2) or Eq. (3) has a large error with the experimental results. And the curvature mutation at point B is ignored in the subsequent analysis. Therefore, this paper proposed a modified geometric model with continuous curvature changes in the deformation zone as shown in Figure 6. Enlightened by the forming radius $(r_C)_Y$ expression given by Eq. (3), the formula of the forming radius r_C is assumed that

$$r_C = t_0\sqrt{\frac{\alpha R_0 + \beta r - \gamma t_0}{t_0}} \tag{6}$$

Where α, β and γ are dimensionless constants that should be determined by fitting the simulation data. The nonlinear relation can be transformed into the linear one by implementing the following changes as shown in Eq. (7).

$$\left(\frac{r_C}{t_0}\right)^2 = \alpha\frac{R_0}{t_0} + \beta\frac{r}{t_0} - \gamma \tag{7}$$

Fifty different groups of the tube initial average radius, the tube initial wall thickness and the die radius were selected using Latin hypercube sampling (LHS). The tube initial average radius ranges from 19 to 35mm, the tube initial wall thickness ranges from 0.8 to 1.5mm and the die radius ranges from 2 to 6mm. Subsequently, the simulation models were established for these fifty specimens in order to obtain their corresponding forming radii. Finally, the appropriate value of the three dimensionless constants were determined by linear curve fitting with MATLAB using the above data.

$\alpha = 0.2984$ β=3.506 γ=6.825

For a specific tube, the critical die radius r_m is determined by solving the equation $r_A = r_C$ of die radius. This indicates that when the die radius is r_m, the forming radius and bending radius are equivalent.

$$r_{\mathrm{m}}=2.253t_0+\sqrt{0.2984R_0t_0-1.998991t_0^2} \tag{8}$$

3.1.2 The Critical Displacement and Maximum Displacement

Since the length of the tube is assumed to remain constant during the inversion process, the critical displacement is determined by the movement of the tube tip F through four points A, B, C and D successively. The arc length $S_{\overset{\frown}{\mathrm{AB}}}$ of segment $\overset{\frown}{\mathrm{AB}}$ can be calculated,

$$S_{\overset{\frown}{\mathrm{AB}}}=\frac{1}{2}\pi r_{\mathrm{A}} \tag{1}$$

Since the curvature is assumed to be linearly distributed in $\overset{\frown}{\mathrm{BC}}$ segment, the average curvature of the segment is,

$$\overline{\kappa}_{\overset{\frown}{\mathrm{BC}}}=\frac{1}{2}\left(\kappa_{\mathrm{A}}+\kappa_{\mathrm{C}}\right) \tag{2}$$

The angle between the tangent lines of point B and point C is $\frac{\pi}{2}$,thus the arc lengths of segment $\overset{\frown}{\mathrm{BC}}$ is,

$$S_{\overset{\frown}{\mathrm{BC}}}=\frac{\pi/2}{\overline{\kappa}_{\overset{\frown}{\mathrm{BC}}}}=\frac{\pi}{\kappa_{\mathrm{A}}+\kappa_{\mathrm{C}}} \tag{3}$$

Similarly, the average curvature and arc length of $\overset{\frown}{\mathrm{CD}}$ segment are,

$$\overline{\kappa}_{\overset{\frown}{\mathrm{CD}}}=\frac{\kappa_{\mathrm{C}}}{2} \tag{4}$$

$$S_{\overset{\frown}{\mathrm{CD}}}=\frac{\pi/2}{\overline{\kappa}_{\overset{\frown}{\mathrm{CD}}}}=\frac{\pi}{\kappa_{\mathrm{C}}} \tag{5}$$

Therefore, the critical displacement of external inversion process is,

$$x_{\mathrm{m}}=S_{\overset{\frown}{\mathrm{AB}}}+S_{\overset{\frown}{\mathrm{BC}}}+S_{\overset{\frown}{\mathrm{CD}}}=\pi\left(0.75r+1.25r_{\mathrm{C}}-0.375t_0\right) \tag{14}$$

The critical displacement, a geometric parameter proposed in this paper to describe inversion geometric models, has not been discussed in previous research. However, the critical displacement corresponding to the geometric models shown in Figure 6 can be calculated according to its definition, respectively:

$$(x_{\mathrm{m}})_H=\frac{3}{4}\cdot 2\pi r_{\mathrm{A}}=1.5\pi\left(r-0.5t_0\right) \tag{6}$$

$$(x_{\mathrm{m}})_N=2\pi r_{\mathrm{A}}=2\pi\left(r-0.5t_0\right) \tag{7}$$

$$(x_{\mathrm{m}})_Y=\frac{1}{4}\cdot 2\pi r_{\mathrm{A}}+\frac{1}{2}\cdot 2\pi r_{\mathrm{C1}}=\pi\left(0.5r+r_{\mathrm{C1}}-0.25t_0\right) \tag{8}$$

Where, $(x_{\mathrm{m}})_H$, $(x_{\mathrm{m}})_N$ and $(x_{\mathrm{m}})_Y$ are the critical displacements obtained by calculating the arc length of $\overset{\frown}{\mathrm{AD}}$ segment in Figure 7a-c, respectively.

The maximum displacement of external inversion process can be determined through the geometric relationship shown in Figure 9 by ignoring the length of segment OD.

$$x_{\max} = 0.5L + 0.5x_{\mathrm{m}} \tag{9}$$

3.2 Force Displacement Curve and Crashworthiness Indicators

Desired criteria considered when assessing crashworthiness are obtained from force-displacement curves. To obtain the theoretical force displacement curve, one should obtain the theoretical steady inversion force, critical displacement and maximum displacement according to Eq. (4). And the theoretical expressions for the critical displacement and the maximum displacement have been derived in Section 3.1. Therefore, theoretical derivation of the steady inversion force is necessary to obtain theoretical force displacement curve.

3.2.1 The steady inversion force

For simplicity, the following basic assumptions are adopted to derive the steady inversion force:

(1) The elastic energy is negligible due to significant plastic deformation. Hence the idealization rigid-perfectly plastic(R-PP) material is employed in the analysis. The flow stress of material is calculated as following (Jiang et al. (2022)):

$$\sigma_0 = \frac{\sigma_{\mathrm{s}} + \sigma_{\mathrm{u}}}{2} \tag{19}$$

Where σ_{s} and σ_{u} are the yield stress and ultimate stress of material, respectively.

(2) The contact between the tube and the die is assumed to be frictionless, and the effect of friction will be discussed later.

(3) Excluding friction, the external work should be equal to the total plastic dissipation according to energy conservation. And the plastic dissipation mainly comprises two plastic deformation mechanisms: bending in the meridional direction (denoted by subscript *l*) and expansion in the circumferential direction (denoted by subscript θ). This is due to El-Domiaty's (1997) demonstration that the sum of these two plastic deformation mechanisms components is approximately 20 times greater than other components.

$$\mathrm{d}W = P \cdot v_0 = \mathrm{d}W_l + \mathrm{d}W_\theta \tag{20}$$

Where, $\mathrm{d}W$ is the external work rate done by the applied compression load P, v_0 is the loading velocity at point A, $\mathrm{d}W_l$ is the plastic energy dissipation rate due to bending in the meridional direction, and $\mathrm{d}W_\theta$ is the plastic energy dissipation rate due to expansion in the circumferential direction.

As shown in Figure 9c, the meridional curvature undergoes an abrupt change at points A and C. Specifically, the curvature of point A changes from zero to κ_{A}, then the bending energy dissipation rate caused by the curvature change at point A is

$$\mathrm{d}W_{l1} = \frac{1}{t_0} M_{\mathrm{P}} \kappa_{\mathrm{A}} S_0 v_0 \tag{21}$$

Where, $M_{\mathrm{p}} = (\sigma_0 t_0^2)/(2\sqrt{3})$ is the fully plastic bending moment (Yao et al. (2018)), $S_0 = 2\pi R_0 t_0$ is the cross-sectional area of the tube. The curvature remains constant in section $\overset{\frown}{\mathrm{AB}}$, resulting in zero bending energy consumption within this segment. While in segment $\overset{\frown}{\mathrm{BC}}$, the curvature gradually changes from κ_{A} (at point B) to κ_{C} (at point C), so a linear distribution of $\kappa(s)$ along s is adopted

$$\kappa(s) = \frac{\kappa_{\mathrm{C}} - \kappa_{\mathrm{A}}}{S_{\overset{\frown}{\mathrm{BC}}}} \left(s - S_{\overset{\frown}{\mathrm{AB}}} \right) + \kappa_{\mathrm{A}} \quad S_{\overset{\frown}{\mathrm{AB}}} \le s \le S_{\overset{\frown}{\mathrm{AB}}} + S_{\overset{\frown}{\mathrm{BC}}} \tag{22}$$

Therefore, the bending energy dissipation rate in segment $\overset{\frown}{\mathrm{BC}}$ is

$$\mathrm{d}W_{l2}=\frac{1}{t_0}M_{\mathrm{P}}\int_{S_{\overline{\mathrm{AB}}}}^{S_{\overline{\mathrm{AB}}}+S_{\overset{\frown}{\mathrm{BC}}}}\left|\frac{\mathrm{d}\kappa(s)}{\mathrm{d}s}\right|S_s v_s \mathrm{d}s \tag{23}$$

Where, S_s and v_s are the cross-sectional area and the loading velocity at coordinate s. According to the volume conservation ($S_s v_s=S_0 v_0$), Eq. (23) can be simplified as

$$\mathrm{d}W_{l2}=2\pi R_0 t_0 \sigma_0 v_0 \begin{cases} \dfrac{t_0}{2\sqrt{3}}\left(\kappa_{\mathrm{A}}-\kappa_{\mathrm{C}}\right) & r_{\mathrm{A}}\le r_{\mathrm{C}} \\ \dfrac{t_0}{2\sqrt{3}}\left(\kappa_{\mathrm{C}}-\kappa_{\mathrm{A}}\right) & r_{\mathrm{A}}> r_{\mathrm{C}} \end{cases} \tag{24}$$

The curvature at point C changes from κ_{C} to zero, then the bending energy dissipation rate caused by the curvature change of point C is

$$\mathrm{d}W_{l3}=\frac{1}{t_0}M_{\mathrm{p}}\kappa_{\mathrm{C}}S_{\mathrm{C}}v_{\mathrm{C}}=\frac{1}{t_0}M_{\mathrm{p}}\kappa_{\mathrm{C}}S_0 v_0 \tag{25}$$

Where S_{C} and v_{C} are the cross-sectional area and the loading velocity at point C. Then the total plastic energy dissipation rate due to bending in the meridional direction is

$$\mathrm{d}W_l=\mathrm{d}W_{l1}+\mathrm{d}W_{l2}+\mathrm{d}W_{l3}=2\pi R_0 t_0 \sigma_0 v_0 \begin{cases} \dfrac{t_0}{\sqrt{3}}\kappa_{\mathrm{A}} & r_{\mathrm{A}}\le r_{\mathrm{C}} \\ \dfrac{t_0}{\sqrt{3}}\kappa_{\mathrm{C}} & r_{\mathrm{A}}> r_{\mathrm{C}} \end{cases} \tag{26}$$

As depicted in Figure 6b, the tube average radius varies from R_0 at point A to R_{C} at point C, thus the circumferential tensile strain is obtained as

$$\varepsilon_\theta=\int_0^{x_{\mathrm{m}}}\frac{dR(s)}{ds}\frac{1}{R(s)}ds=\ln\frac{R_0+r+r_{\mathrm{C}}-0.5t_0}{R_0} \tag{27}$$

Therefore, the plastic energy dissipation rate due to expansion in the circumferential direction is

$$\mathrm{d}W_\theta=S_0 v_0 \sigma_0 \varepsilon_\theta=2\pi R_0 t_0 v_0 \sigma_0 \ln\frac{R_0+r+r_{\mathrm{C}}-0.5t_0}{R_0} \tag{28}$$

Inserting Eq. (26) and Eq. (28) into Eq. (20), the steady inversion force without considering the friction effect is expressed as a function.

$$P_{\mathrm{m}}=2\pi R_0 t_0 \sigma_0 \begin{cases} \dfrac{t_0}{\sqrt{3}r_{\mathrm{A}}}+\ln\dfrac{R_0+r+r_{\mathrm{C}}-0.5t_0}{R_0} & r_{\mathrm{A}}\le r_{\mathrm{C}} \\ \dfrac{t_0}{\sqrt{3}r_{\mathrm{C}}}+\ln\dfrac{R_0+r+r_{\mathrm{C}}-0.5t_0}{R_0} & r_{\mathrm{A}}> r_{\mathrm{C}} \end{cases} \tag{29}$$

To simplify the theoretical derivation, the friction effect between the tube and the die was not considered in the above theoretical analysis. However, it should be noted that the friction at the contact area can greatly influence inversion mode and even prevents the tube from inversion successfully. Previous theoretical models (Niknejad and Moeinifard (2012), Yu et al. (2016)) based on energy method did not consider the friction energy consumption. By referring to the theoretical model (Liu et al. (2018)), the refined steady inversion force P_{mf} considering friction effect is,

$$P_{mf} = e^{\frac{\pi}{2}f} P_{m} \tag{30}$$

Where f is the friction coefficient between the tube and the die.

In the process of calculating the steady inversion forces, Niknejad and Moeinifard (2012) and Yu et al. (2016) neglected the friction effect and the different flow stress are adopted in the previous three model. For consistency, the flow stress defined by Eq. (19) is uniformly adopted and the friction effect is considered as the current model to obtained the steady inversion force $(P_m)_H$, $(P_m)_N$, $(P_m)_Y$, which corresponding to references Huang and Yu (1996), Niknejad and Moeinifard (2012) and Yu et al. (2016) respectively.

$$(P_m)_H = 2\pi R_0 t_0 \sigma_0 \left(\frac{t_0}{2r - t_0} + \ln \frac{R_0 + 2r - t_0}{R_0} \right) e^{\frac{\pi}{2}f} \tag{31}$$

$$(P_m)_N = 2\pi R_0 t_0 \sigma_0 \left(\frac{t_0}{4r - 2t_0} + \frac{t_0}{4R_0} + \frac{2r - t_0}{R_0} + \frac{t_0}{4R_0 + 8r - 4t_0} + \frac{2r - t_0}{R_0 + 2r - t_0} \right) e^{\frac{\pi}{2}f} \tag{10}$$

$$(P_m)_Y = 2\pi R_0 t_0 \sigma_0 \left(\frac{t_0}{4r - 2t_0} + \frac{t_0}{4r_{C1}} + \frac{r - 0.5t_0}{R_0} + \frac{r_{C1}}{R_0 + r - 0.5t_0} \right) e^{\frac{\pi}{2}f} \tag{11}$$

3.2.2 The Total Energy Absorption and The Specific Energy Absorption

The total energy absorption E_a (represented by the area under the force–displacement curve) can be calculated through integration of Eq. (4).

$$E_a = \int_0^{x_{max}} P(x)dx = \frac{2}{3} P_{mf} x_m + P_{mf}(x_{max} - x_m) \tag{12}$$

Among various indicators, the specific energy absorption (*SEA*) is commonly used to quantify the energy absorption capacity of unit structural materials as,

$$SEA = \frac{E_a}{M} \tag{13}$$

Where M is the total mass of the structure.

4. RESULTS AND DISCUSSION

4.1 Validation of The Theoretical Model

The forming radii of the geometric modes proposed by Huang and Yu (1996) (Figure 7a) and Niknejad and Moeinifard (2012) (Figure 7b) are determined by Eq. (2). And the forming radius of the geometric modes proposed by Yu et al. (2016) (Figure 7c) is determined by Eq. (3). For comparison, the experimental results and various theoretical results are shown in Figure 8. It should be noted that the forming radius defined by Eq. (2) solely depends on the tube wall thickness and the die radius, but not on the tube radius. That is the forming radii of cases Ar3EX, Br3EX and Cr3EX obtained by Huang and Yu (1996)] and Niknejad and Moeinifard (2012) are all identical due to the same tube thickness and die radius, which is obviously

inconsistent with the experimental results. For the four cases shown in Figure 8, the forming radii obtained by Eq. (3) proposed by Yu et al. (2016) are smaller than the experimental results. It can be seen that the predicted forming radius by current model are much closer to the experimental results than the other three models.

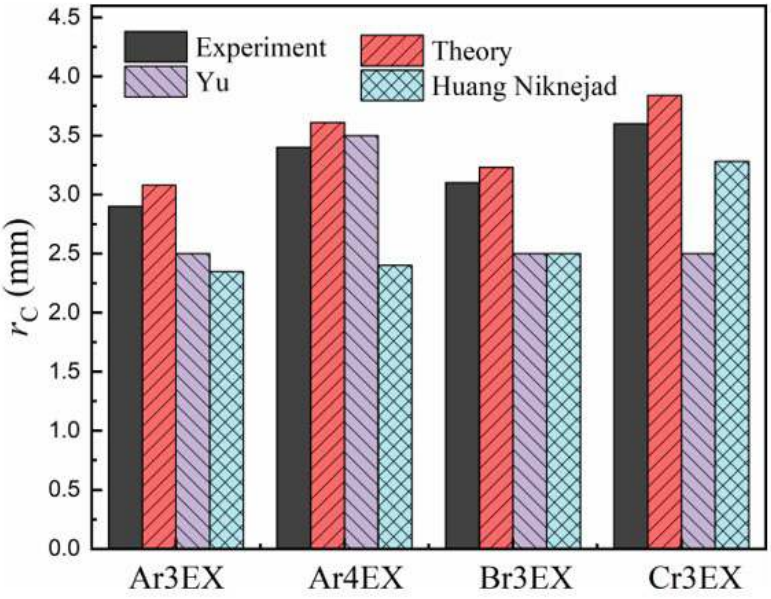


Figure 8 Comparisons of the experimental and the different theoretical results of the forming radius

Figure 9 shows the relationship of the difference value between the forming radius and the bending radius versus the die radius for tube A and C. It can be inferred that a critical die radius r_m is obtained by Eq. (8). When the die radius is smaller than this critical value, the forming radius is bigger than the bending radius; conversely, when it is larger than this critical value, the forming radius is smaller than the bending radius. And the critical die radius varies among different tubes: $(r_m)_A = 4.21\text{mm}$ for tube A, $(r_m)_B = 4.42\text{mm}$ for tube B and $(r_m)_C = 5.72\text{mm}$ for tube C. This finding is also consistent with the trend obtained by experiments and finite element.

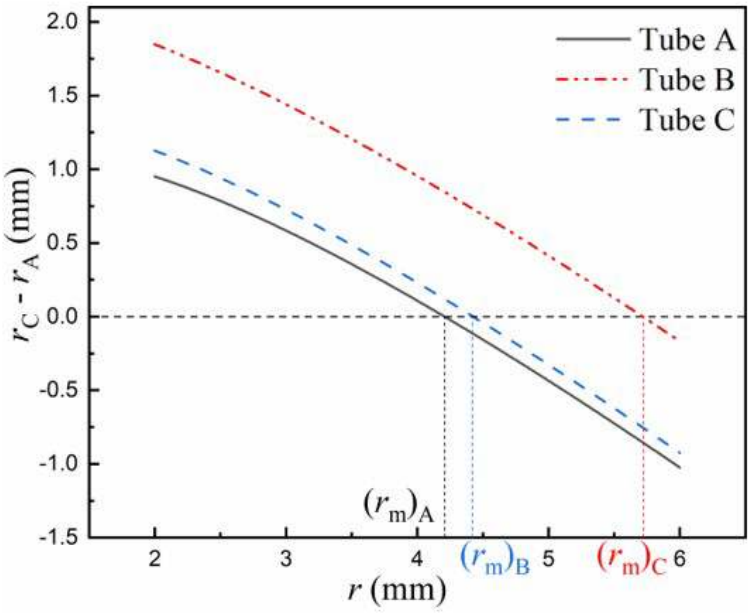


Figure 9 The difference value between the forming radius and the bending radius versus die radius

The critical displacement of current model is determined by Eq. (14). The critical displacements corresponding to Eqs. (15-16) are calculated according to the three different geometric models in Figure 7. The obtained results are summarized and compared in Figure 10, revealing that the predicted critical displacement by Eq. (14) is meaningfully better than the results obtained by Eqs. (15-16).

The comparison between numerical and different theoretical results for the steady inversion force with respect to die radius is displayed in Figure 11. It is observed that the theoretical model proposed by Niknejad (Eq. (32)) exhibits significant deviation from the other three models, the error of this theoretical results becomes larger as the radius of the die increases. And the other three models demonstrate nearly identical behavior when the die radius is bigger than the critical die radius r_m, while the current model aligns more closely with simulation results when the radius is smaller than the critical die radius r_m. In most cases, the theoretical prediction based on Huang's hypothesis (Eq. (31)) and Yu (Eq. (33)) are lower than the numerical result. Comparing the previous three models, the theoretical predictions of the steady inversion force obtained by present analytical model are in better agreement with the simulation results.

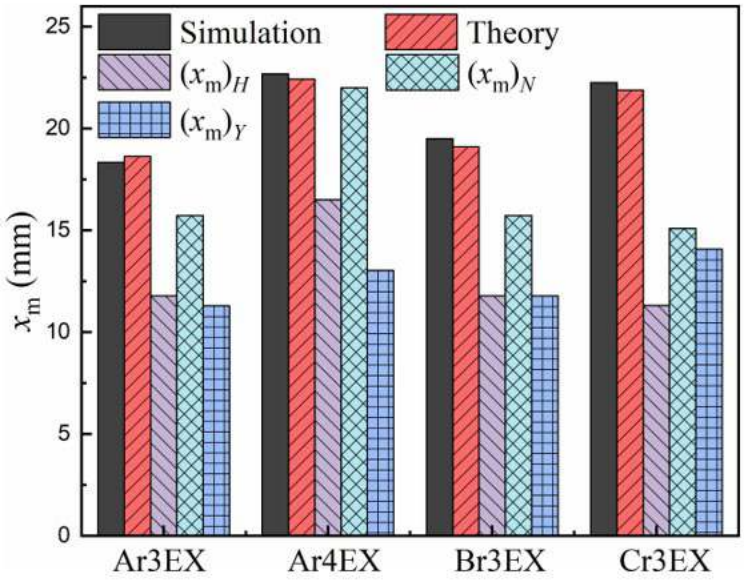


Figure 10 Comparisons of the simulation and different theoretical results of the critical displacement

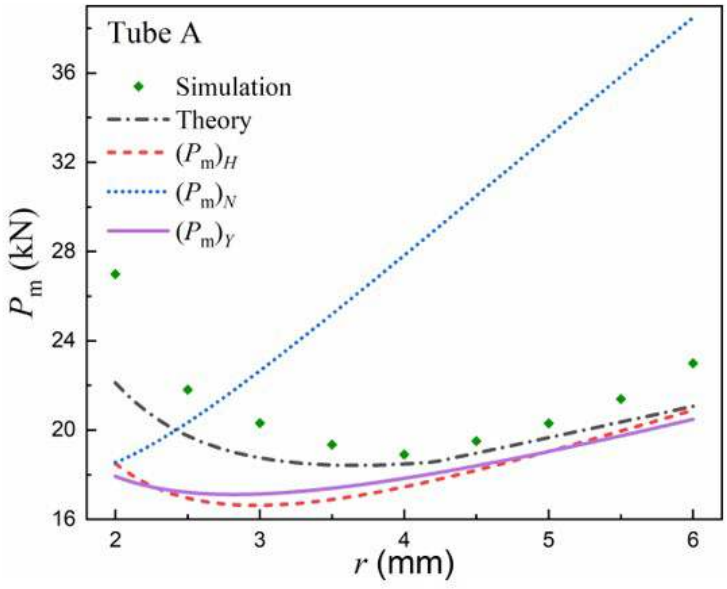


Figure 11 Comparison of the theoretical predictions with simulation results for the steady inversion force

Figure 12 presents a comparison of the inversion force versus displacement obtained by experiment test, FE simulation and theoretical model. It is observed that the experimental, numerical and analytical results agree well with each other. The steady inversion forces obtained by Eqs. (31-33) under corresponding experimental conditions are also shown in Figure 12. It is evident that the current theoretical model can predict the steady inversion force well.

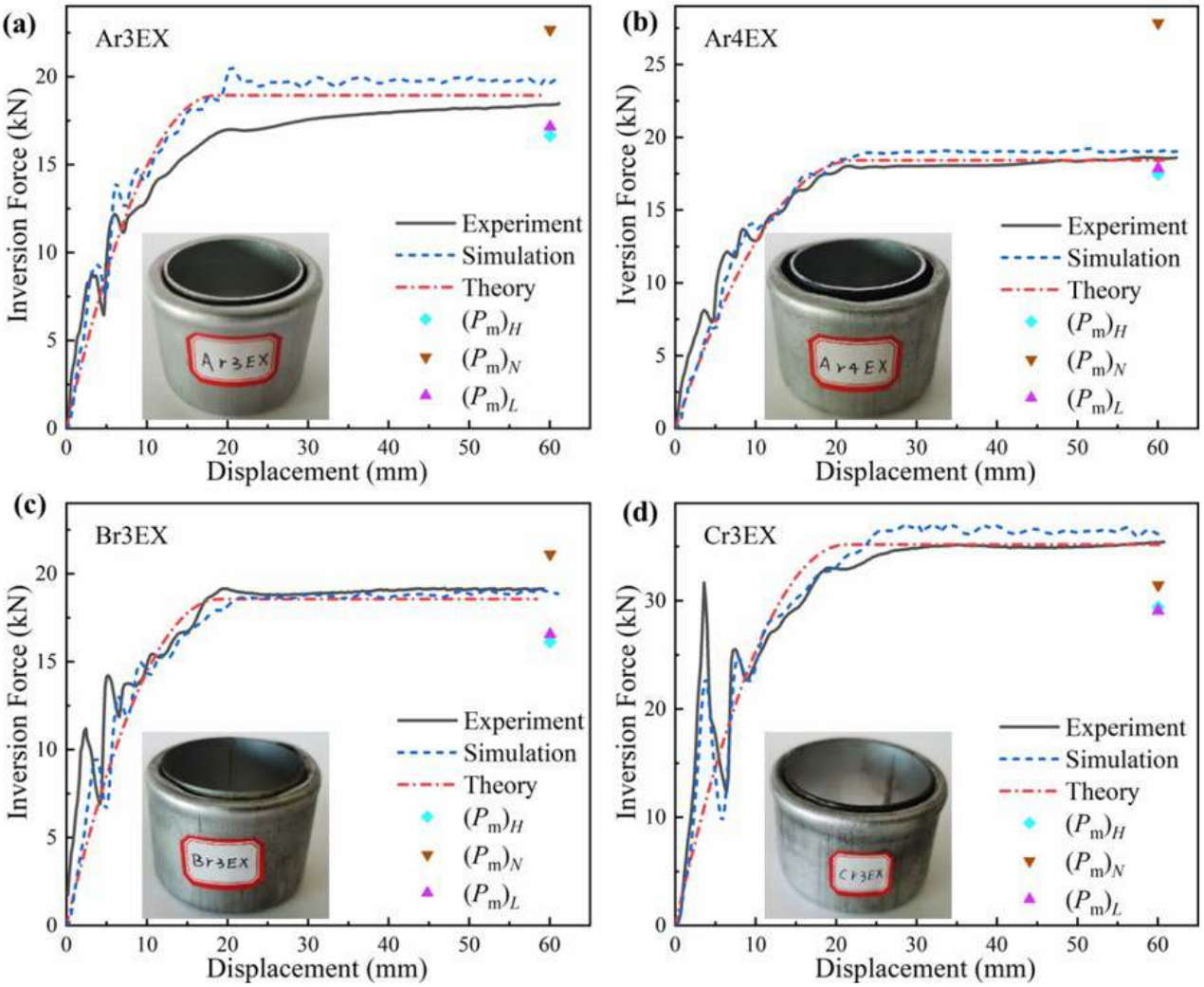


Figure 12 Comparisons of the theoretical predictions with simulation and experiment results for force displacement curves: (a)Ar3EX (b) Ar4EX (c)Br3EX (d) Cr3EX

4.2 Plastic Deformation Mechanisms

Except for friction, two types plastic deformation mechanisms are considered in current theoretical models to obtain the steady inversion force. The corresponding contributions to the steady inversion force are P_l^b and P_θ^e. According to Eq. (29), these two force components can be calculated as follows,

$$\begin{cases} P_l^b = 2\pi R_0 t_0 \sigma_0 \begin{cases} \dfrac{t_0}{\sqrt{3} r_A} & r_A \le r_C \\ \dfrac{t_0}{\sqrt{3} r_C} & r_A > r_C \end{cases} \\ P_\theta^e = 2\pi R_0 t_0 \sigma_0 \cdot \ln \dfrac{R_0 + r + r_C - 0.5 t_0}{R_0} \end{cases} \tag{14}$$

According to Eq. (31) and Eq. (32), the theoretical prediction based on Huang's hypothesis and Yu's also considered these two deformation mechanisms. And the force components can be calculated as follows,

$$\begin{cases} (P_l^b)_H = 2\pi R_0 t_0 \sigma_0 \cdot \dfrac{t_0}{2r - t_0} \\ (P_\theta^e)_H = 2\pi R_0 t_0 \sigma_0 \cdot \ln \dfrac{R_0 + 2r - t_0}{R_0} \end{cases} \tag{15}$$

$$\begin{cases} (P_l^b)_Y = 2\pi R_0 t_0 \sigma_0 (\dfrac{t_0}{4r - 2t_0} + \dfrac{t_0}{4r_{C1}}) \\ (P_\theta^e)_Y = 2\pi R_0 t_0 \sigma_0 (\dfrac{r - 0.5t_0}{R_0} + \dfrac{r_{C1}}{R_0 + r - 0.5t_0}) \end{cases} \tag{16}$$

Where the subscripts *H* and *Y* denoted the theoretical prediction based on Huang's hypothesis (Eq. (31)) and Yu's (Eq. (33)), respectively. In addition to the two deformation mechanisms mentioned above, the theoretical model of Niknejad also considers two more deformation mechanisms: bending and reduction in the circumferential direction. And the corresponding contributions to the steady inversion force are P_θ^b and P_θ^r, respectively. The force components determined by this theoretical model are calculated as follows,

$$\begin{cases} (P_l^b)_N = 2\pi R_0 t_0 \sigma_0 \cdot \dfrac{t_0}{4r - 2t_0} \\ (P_\theta^e)_N = 2\pi R_0 t_0 \sigma_0 \cdot \dfrac{2r - t_0}{R_0} \\ (P_\theta^b)_N = 2\pi R_0 t_0 \sigma_0 (\dfrac{t_0}{4R_0} + \dfrac{t_0}{4R_0 + 8r - 4t_0}) \\ (P_\theta^r)_N = 2\pi R_0 t_0 \sigma_0 \cdot \dfrac{2r - t_0}{R_0 + 2r - t_0} \end{cases} \tag{17}$$

The forces calculated for the corresponding experimental conditions by Eqs. (36-39) are listed in Table 5. It can be observed that the P_θ^e of the four models exhibit a similar value. The mainly reason for the significantly difference between theoretical model proposed by Niknejad with the other three models lies in the fact that the steady inversion force proposed by Niknejad takes P_θ^b and P_θ^r into account more than the other three models, while P_θ^b is much smaller than other force components and can be neglected, and P_θ^r, caused by reduction in the circumferential direction of $\overset{\frown}{\mathrm{CD}}$ segment, only affects the inversion force in the bending stage and does not contribute to the steady inversion force in the steady stage. The other reason is that $(P_l^b)_N$ only the force contributed by the meridional bending at point A is considered in Niknejad's model, while the other three models all take into account the bending at two points A and C or in the segment $\overset{\frown}{\mathrm{AC}}$. Therefore, $(P_l^b)_N$ is only about half of the other three models' force components caused by the meridional bending. Except for Niknejad's model, the other three model only consider P_l^b caused by the bending at two points A and C or in the segment $\overset{\frown}{\mathrm{AC}}$ and P_θ^e caused by expansion in the circumferential direction of segment $\overset{\frown}{\mathrm{AC}}$ when calculating the steady inversion force. The discrepancy among the other three models is primarily attributed to differences in forming radius, which has been validated in Section 5.1. Therefore, it can be inferred that the current theoretical predictions of the steady inversion force (Eq. (29)) show a roughly agreement with both experimental and simulation results.

Table 5 The contributions of different deformation mechanisms to the steady inversion force

Test case		P_l^b (kN)	P_θ^e (kN)	P_θ^b (kN)	P_θ^r (kN)	P_m (kN)
Ar3EX	Theory	7.09	7.73	0	0	14.82
	Huang	6.14	7.01	0	0	13.15
	Niknejad	3.07	7.87	0.71	6.26	17.91
	Yu	6.34	7.21	0	0	13.55
Ar4EX	Theory	5.06	9.54	0	0	14.6
	Huang	4.38	9.41	0	0	13.79
	Niknejad	2.19	11.02	0.68	8.11	22
	Yu	5.39	8.71	0	0	14.1
Br3EX	Theory	7.35	7.21	0	0	14.56
	Huang	6.36	6.38	0	0	12.74
	Niknejad	3.18	7.07	0.64	5.78	16.67
	Yu	6.36	6.72	0	0	13.08
Cr3EX	Theory	17.45	10.35	0	0	27.8
	Huang	15.11	8.12	0	0	23.23
	Niknejad	7.55	8.69	1.02	7.59	24.85
	Yu	13.09	9.88	0	0	22.97

4.3 Energy Absorption Characteristics

In order to better understand the energy absorption behavior of external inversion tubes, the effects of several typical parameters on the crashworthiness are expounded. The performance of an energy absorber is frequently evaluated or compared through crashworthiness criteria, which are obtained from force-displacement curves. And the force-displacement curve obtained by current theoretical model were compared and validated by experimental results, simulation results and previous theoretical model in the above discussion. Therefore, the current model can be used to discuss the energy absorption characteristics of the external inversion mode over a circular die. Material properties of tube A are used in this section for more general evaluation of energy absorption characteristics. The effects of tube average radius R_0, wall thickness t_0, and die radius r on the inversion tube were presented in Figure 13. The tube average radius R_0 ranges from 19 to 35mm, the wall thickness t_0 ranges from 0.8 to 1.5mm and the die radius r ranges from 2 to 6mm.

Figure 13a-c demonstrates that when the die radius is bigger than the critical radius r_m, the three crashworthiness criteria increases monotonically with respect to the die radius, and when the die radius is smaller than the critical radius, there is an optimal die radius r_{oP} that minimizes the steady inversion force for the metal tube. Since Eq. (29) gives an explicit function of the steady inversion force respect to the die radius when the die radius is smaller than the critical radius, thus

$$\frac{\mathrm{d}P_m(r_A \le r_C)}{\mathrm{d}r} = \frac{\mathrm{d}\dfrac{t_0}{\sqrt{3}r_A} + \ln\dfrac{R_0 + r + r_C - 0.5t_0}{R_0}}{\mathrm{d}r} \tag{18}$$

$$= \frac{1 + \dfrac{1.2555t_0}{\sqrt{0.2984R_0t_0 + 3.506rt_0 - 6.825{t_0}^2}}}{R_0 + r - 0.5t_0 + \sqrt{0.2984R_0t_0 + 3.506rt_0 - 6.825{t_0}^2}} - \frac{t_0}{\sqrt{3}(r - 0.5t_0)^2} = 0$$

will lead to the force optimized radius of r_{oP}. Similarly,

$$\frac{\mathrm{d}E_a(r_A \le r_C)}{\mathrm{d}r} = \frac{\mathrm{d}SEA(r_A \le r_C)}{\mathrm{d}r} = 0 \tag{19}$$

will lead to the energy optimized radius r_{oE} that minimizes the total energy absorption and the specific energy absorption. The force optimal radius r_{oP} is consistently slightly smaller than the critical radius r_m, and the energy optimized radius of r_{oE} is consistently slightly smaller than the force optimal radius r_{oP} as shown in Table 6.

Table 6 The optimal radius and the critical radius for different tubes

R_0 (mm)	t_0 (mm)	r_m (mm)	r_{oP} (mm)	r_{oE} (mm)
20	1	4.25	3.70	3.5
25	1	4.59	4.09	3.86
30	1	4.89	4.44	4.18

According to Figure 13d-f, an increase in the tube wall thickness t_0 will significantly increase all the three energy absorption characteristics. Moreover, when the die radius is small, the energy absorption characteristics exhibit a rapid growth with increasing wall thickness; whereas for large die radii, the energy absorption characteristics demonstrate a slower rate of improvement with increased thickness.

The tube average radius R_0 will significantly increase the steady inversion force and the total energy absorption as shown in Figure 13g-i. However, the specific energy absorption (*SEA*) has a monotonically decreasing relationship with the tube average radius due to the effects of the mass. An ideal energy absorber always seeks to achieve greater energy absorption and specific energy absorption simultaneously. Therefore, the *SEA* and E_a need to be balanced when changing the tube average radius to improve the crashworthiness of the energy absorber.

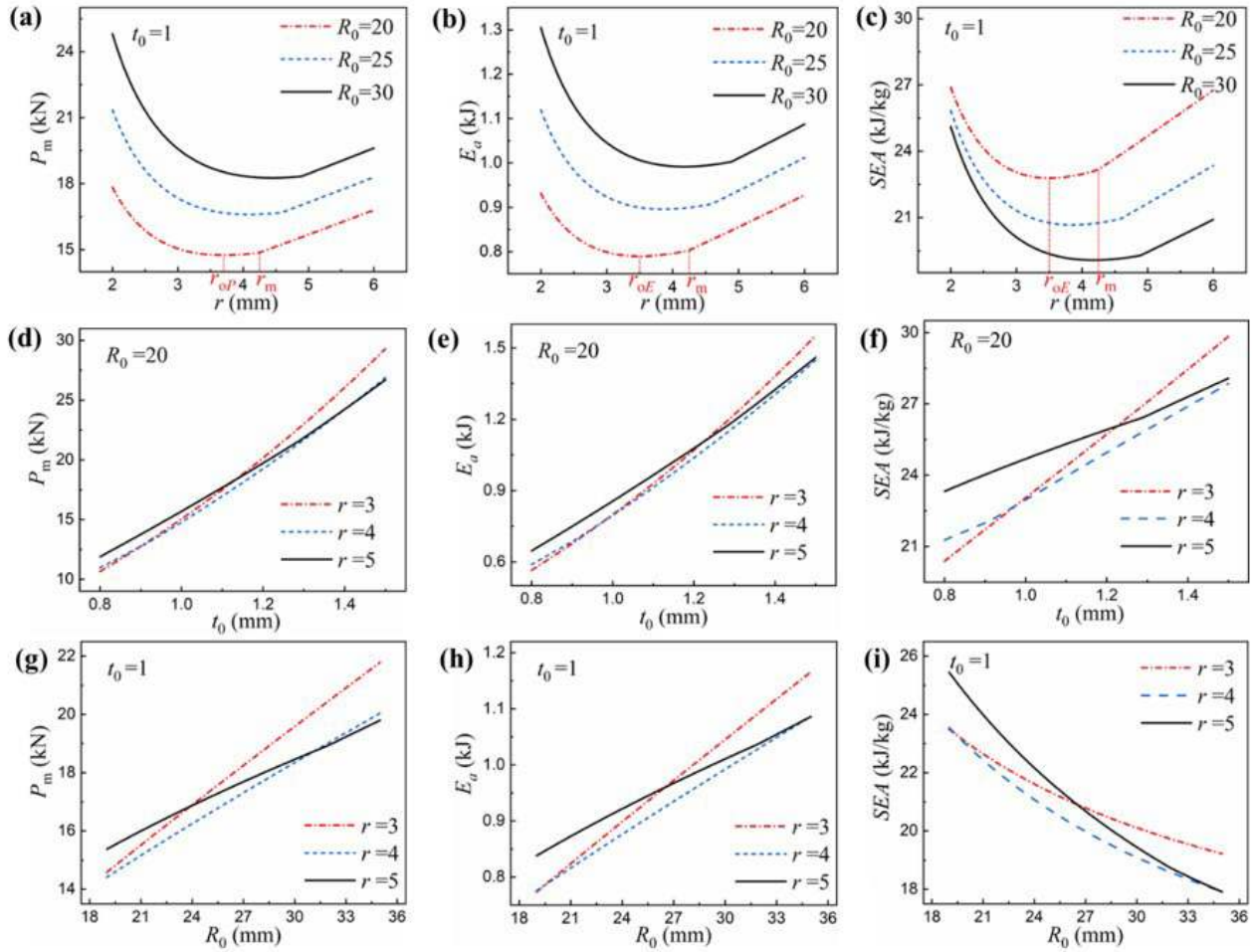


Figure13 Theoretical results of the crashworthiness indicators versus geometrical parameters: (a) P_m - r ; (b) E_a - r ; (c) SEA - r ; (d) P_m - t_0 ; (e) E_a - t_0 ; (f) SEA - t_0 ; (g) P_m - R_0 ; (h) E_a - R_0 ; (i) SEA - R_0

5 CONCLUSION

In this research, a revised theoretical model considering the curvature change in deformation area is proposed and the reliability of the theoretical model is validated by experiments and simulation. Further, energy absorption mechanisms and crashworthiness of the inversion tube were estimated based on the theoretical model. The following conclusions may be drawn:

(1) The experimental and simulation results divulged that the curvature in deformation area is varying and the inversion process was divided into two stages by three states.

(2) Compared with the previous geometric model, the present model greatly improves the prediction accuracy of the forming radius, the critical radius and the maximum displacement. Due to the accurate prediction of the forming radius and the segmentation calculation according to the die radius, the steady inversion force is proposed with large accuracy.

(3) The present theoretical model can predict the inversion force of the whole inversion process, and then the theoretical results of the total and specific energy absorption can be obtained.

(4) The three crashworthiness indicators (the steady inversion force, the total energy absorbed and the specific energy absorption) are dependent on the wall thickness, the tube radius and the die radius. The three crashworthiness indicators all increase with the increase tube wall thickness. However, SEA decrease with the increase tube average radius. Furthermore, there exists a force optimized radius of r_{oP} that minimizes the steady inversion force and an energy optimized radius r_{oE} that minimizes the total energy absorption and the specific energy absorption.

Author's Contribuitions: Conceptualization, Methodology and Writing - original draft, Wanqi Zhang; Writing - review & editing, Guansheng Yin; Investigation, Minghui Shi and Pengfei Wei; Resources, Jianqiang Wang; Supervision, Junkai Zhao.

Editor: Marcílio Alves

References

Al-Hassani S.T.S, Johnson W, Lowe WT., (1972). Characteristics of Inversion Tubes under Axial Loading. Journal of Mechanical Engineering Science, 14(6):370-381.

Amirhosein M., Pouya A., Hossein D., (2022). Experimental and Numerical Crushing Analysis of a Novel Multibody Thin-Walled Circular Tube Under Axial Impact Loading. International Journal of Applied Mechanics, 14(09):2250042

Ben Jiang, Xueyan Chen, Jianxin Yu. (2022). Energy-absorbing properties of thin-walled square tubes filled with hollow sphere. Thin-Walled Structures,180:109765.

Bowen Tan, Shuguang Yao, Lin Zhang. (2023). A novel deformation mode of expansion tubes accounting for extra contact. International Journal of Mechanical Sciences, 242:108024

El-Domiaty A. (1997). Curling of thin tubes: Analytical and experimental study Journal of Materials Engineering and Performance, 6(4):481-495.

Fauzan Djamaluddin F., (2023). Crash behavior and optimization of double tubes with different cross section. International Journal of Crashworthiness, 28(2):280-287

Huang Zaowen, Yu Yanqin. (1996). Analysison the invertube load and the affective factors under axial pressure[J]. China Mechanical Engineering,7(01): 75-77.

Jiafeng Song, Shucai Xu, Jianfei Zhou. (2021). Experiment and numerical simulation study on the bionic tubes with gradient thickness under oblique loading. Thin-Walled Structures, 163(2):107624.

Leu D K. (2000). The curling characteristics of static inside-out inversion of metal tubes. International Journal of Machine Tools and Manufacture, 40(1): 65-80.

Liu YuZhe, Qiu XinMing, Yu T.X. (2018). A theoretical model of the inversion tube over a conical die. Thin-Walled Structures, 127:31-39.

Luo Yunhua, Huang Zaowen, Zhang Xianglin. (2003). Study on deforming mechanism of circular tube outside inversion under pressed axially[J]. Forging & Stamping Technology, 28(05):54-57.

Magrinho J P, Centeno G, Silva M B., (2019). On the formability limits of thin-walled tube inversion using different die fillet radii. Thin-Walled Structures, 144:106328.

Miscow PC, Al-Qureshi H A. (1997). Mechanics of static and dynamic inversion processes. International Journal of Mechanical Sciences, 39(2):147-161.

Na Qiu, Depei Wang, Yajie Li. (2023) Influence of spherical triggers on axial collapse of tapered tubes. International Journal of Crashworthiness. DOI:10.1080/13588265.2023.2183791

Niknejad A, Moeinifard M. (2012). Theoretical and experimental studies of the external inversion process in the circular metal tubes. Materials and Design, 40: 324-330.

Ruyang Y., Tong P., and Bei Zhang., (2023). On the crashworthiness of thin-walled multi-cell structures and materials: State of the art and prospects. Thin-Walled Structures, 189:110734

Shilong Wang, Min Zhang, Yao Wang. (2021). Experimental studies on quasi-static axial crushing of additively-manufactured PLA random honeycomb-filled double circular tubes. Composite Structures,261:113553.

Xinming Q, Mingle P., Xiaohuan Y. (2016). Analysis of the energy absorption properties for tubular structure under compression of different failure modes. Mechanics in Engineering, 38(05): 477-492.

Yao R Y, Yin G S, Hao W Q. (2018). Axial buckling modes and crashworthiness of circular tube with external linear gradient grooves. Thin-Walled Structures, 134: 395-406.

Yu XH, Qiu XM, Yu TX. (2016). Theoretical model of a metal tube under inversion over circular dies[J]. International Journal of Mechanical Sciences. 2016, 108-109:23-28. DOI:10.1016/j.ijmecsci.2016.01.028</jrn>